J|A|C|S JOURNAL OF THE AMERICAN CHEMICAL SOCIETY

Article

pubs.acs.org/JACS

Structure/Processing/Properties Relationships in Nanoporous Nanoparticles As Applied to Catalysis of the Cathodic Oxygen Reduction Reaction

Joshua Snyder,[†] Ian McCue,[†] Ken Livi,[‡] and Jonah Erlebacher*[,†]

[†]Department of Materials Science and Engineering & Department of Chemical and Biomolecular Engineering and [‡]Department of Earth and Planetary Sciences, Johns Hopkins University, Baltimore, Maryland 21218, United States

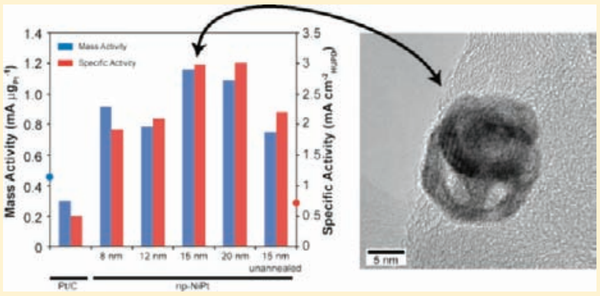

ABSTRACT: We present a comprehensive experimental study of the formation and activity of dealloyed nanoporous Ni/Pt alloy nanoparticles for the cathodic oxygen reduction reaction. By addressing the kinetics of nucleation during solvothermal synthesis we developed a method to control the size and composition of Ni/Pt alloy nanoparticles over a broad range while maintaining an adequate size distribution. Electrochemical dealloying of these size-controlled nanoparticles was used to explore conditions in which hierarchical nanoporosity within nanoparticles can evolve. Our results show that in order to evolve fully formed porosity, particles must have a minimum diameter of ~15 nm, a result consistent with the surface kinetic processes occurring during dealloying. Nanoporous nanoparticles possess ligaments and voids with diameters of approximately 2 nm, high surface area/mass ratios usually associated with much smaller particles, and a composition consistent with a Pt-skeleton covering a Ni/Pt alloy core. Electrochemical measurements show that the mass activity for the oxygen reduction reaction using carbon-supported nanoporous Ni/Pt nanoparticles is nearly four times that of commercial Pt/C catalyst and even exceeds that of comparable nonporous Pt-skeleton Ni/Pt alloy nanoparticles.

1. INTRODUCTION

Meeting the world's rapidly increasing demand for energy requires development of secure, reliable, renewable, and sustainable sources of energy and is one of the greatest and most important challenges facing the scientific community in the 21st century. There is only a very small probability of a "silver bullet" solution for fulfillment of this energy demand, and the most realistic approach involves customized energy plans in which sources and supply are individually tailored for each geographical/geopolitical region of the world. In any proposed plan, fuel cells will likely play a significant role as their relatively high-energy conversion efficiencies, ~50%,[1] and their ability to use high-energy density fuels such as methanol (20 MJ kg^{-1}) and hydrogen (140 MJ kg^{-1})[2] make them attractive energy extraction devices for both stationary and mobile applications. The key and limiting chemical process with regard to fuel cell efficiency is the cathodic oxygen reduction reaction (ORR) where oxygen is reduced to water through the simultaneous transfer of four electrons and four protons and is only effectively driven by expensive Pt nanoparticle-based catalysts.[1,3−5] Widespread commercial integration of fuel cells requires significant improvements in activity for Pt-based catalysts in order to lower required loadings and minimize cost. Recent progress in this area has been focused on Pt−transition metal alloy nanoparticle catalysts with compositional gradients that exhibit improved ORR activities in comparison to traditional supported Pt/C catalysts.[6−13]

Catalyst development has been guided by experimental and theoretical work on Pt−transition metal single-crystal and polycrystalline planar surfaces where the optimum structure is that of a Pt-skin protecting a Pt−transition metal alloy.[6,7,14−16] Transition metal atoms in the underlying atomic layers induce a downshift in the d-band center of the surface Pt atoms as well as a change in the geometric structure of the surface resulting in an optimized interaction between Pt and intermediate oxide species of the ORR, preventing surface poisoning and freeing Pt sites for further O_2 adsorption and reduction.[6,14,16] Pt-skin structures are formed through thermal annealing which induces subsurface Pt to segregate to the surface forming a smooth protective skin.[6,7,14,16] This structure differs from that of core−shell catalysts which are made intentionally through one of two techniques: (1) deposition of one Pt monolayer at a time on a transition metal/alloy core through galvanic displacement of a sacrificial underpotentially deposited metal monolayer and (2) depletion of the transition metal from the outermost atomic layers of Pt-alloy nanoparticles through chemical or electrochemical etching forming a rough Pt-skeleton surface. Pt-monolayer catalysts made through galvanic displacement have been shown to be very active on a per Pt mass basis because there is no Pt hidden within the core of the nanoparticles; all Pt is surface Pt and potentially active.[8,9,12,17−19] Electrochemical dealloying of Pt-alloy nanoparticles is a less experimentally

Received: February 27, 2012
Published: April 25, 2012

dx.doi.org/10.1021/ja3019498 | *J. Am. Chem. Soc.* 2012, 134, 8633−8645

intensive process by which core–shell catalysts may be formed. Transition metal atoms are etched from the outermost atomic layers of Pt–transition metal alloy nanoparticles under applied potential or potential cycling, enriching the surface in Pt but also maintaining a significant residual fraction of the transition metal within the core of the particle.[7,20−26] Typically, three-dimensional (3D) porosity does not evolve in these types of catalysts because in most cases the composition ratio of Pt to transition metal is too high and the initial particle sizes are typically too small.

1.1. Porosity in Nanoparticles. Fully formed, 3D porosity can be catalytically advantageous where structural nanoporosity results in high surface area to volume ratios and creates a confined reaction environment which could potentially lead to higher attempt frequencies or higher preexponential factors under Arrhenius kinetics, resulting in overall improved reaction kinetics.[27−30] The dealloying mechanism—selective dissolution of the less-noble component from a binary or multicomponent solid solution at a potential at which the remaining more-noble component is free to diffuse along the surface by which 3D porosity evolves[31,32]—intrinsically forms a core–shell nanoporous structure where the surface is passivated by the more-noble component and the interior of the ligaments maintain a significant residual fraction of the less-noble component. In this case, dealloying is relevant not in terms of degradation or corrosion but may be used as a tool to develop new nanostructured catalysts. Planar nanoporous metals have already proven very active for the ORR,[33] but if dealloying is to be used in fuel cell catalyst synthesis the nanoporous materials must be engineered into a form factor that may be readily integrated into fuel cell cathode catalyst layers, namely, forming nanoporosity on a nanoparticulate scale. This is the subject of this manuscript

Porosity in Pt alloy nanoparticles has been found to unintentionally evolve in situ under load cycling, i.e., repeated variation from reductive to oxidative potentials, during fuel cell operation or in a half-cell during electrochemical activity measurements for both PtCo and PtCu alloy nanoparticles.[4,20,34,35] The catalysts in these cases consisted of alloy particles with a large dispersion of particle sizes as a consequence of their preparation procedures, typically salt impregnation of a carbon support followed by high-temperature reduction with hydrogen. Therefore, porosity was formed in only a selection of the larger particles where the smaller particles likely quickly formed a passive Pt surface layer after depletion of the alloying component from the outermost atomic layers. This inconsistency in particle morphology can negatively affect both the electrochemically active surface area (ECSA) and the electrocatalytic activity of the catalyst. More concerted efforts have been made to develop nanoporous nanoparticles by dealloying of Cu-rich Pd and Pt alloys.[36,37] Here, again, particles were initially formed through salt impregnation, and the resulting particle sizes ranged from 2 to 25 nm. Therefore, the final dealloyed catalyst contained a significant fraction of solid/nonporous nanoparticles. Copper as a transition metal alloying component suffers in terms of both activity and stability compared to other alloying components such as Ni.[38−40] Li et al.[41] recently optimized a solvothermal synthesis process from which they were able to make 20 nm, Ni-rich Pt alloy nanoparticles with a minimal distribution in average particle diameter. These particles were dealloyed as made, without an additional annealing step, through free corrosion in concentrated HNO_3, and formed porous particles. No oxygen reduction activity was reported. As we will show in our study, annealing is a critical step in the process of forming active nanoporous nanoparticles as it helps to homogeneously disperse the alloying components within each particle and leads to a greater retention of residual Ni, resulting in improved performance. Also, the use of free corrosion will result in a rough surface which is not ideal for the ORR as a high density of low-coordination sites has been shown to negatively affect ORR activity.[42] In contrast, dealloying through potential cycling electrochemically anneals the surface of the porous structure smoothening out roughness and decreasing the density of low-coordination sites. The nanoparticle synthesis procedure in ref 41 is also limited in its ability to reliably control particle size. In short, nanoporous nanoparticles have been demonstrated in the literature, but there has not been a comprehensive study of their synthesis and properties. With a goal here to form nanoporous Ni/Pt nanoparticles active toward the ORR, we needed to modify/develop a chemical synthesis procedure that facilitated control of both size and composition over a wide range while maintaining an adequate size distribution. This allowed us to study the effect of particle size on dealloying and porosity formation and properly tune morphology and composition for optimal catalytic activity.

1.2. Solvothermal Synthesis. Solvothermal reductive synthesis has evolved to be one of the more versatile and powerful techniques for fabrication of metal and metal alloy[43−46] nanostructures allowing superior control of shape/morphology, size, size distribution, and composition,[47−55] each of which have a direct effect on the physical and chemical properties of the formed nanostructures. The most common procedures for solvothermal synthesis of nanoparticles involve dissolution and subsequent reduction of organic ligated metallic salts in high boiling point organic solvents commonly containing long chain amine and/or carboxylic acid capping agents and one or more reducing agents. The organic capping agents aid in the control of size, shape, and size distribution not only through adsorption and interaction with reduced metallic species on the surface of the growing nanocrystals but also through formation of metal ion/capping agent complexes resulting in adjustments in the rates of nucleation and growth.[56−60] The vast majority of nanoparticle synthesis procedures are focused on fast nucleation that is quickly quenched, effectively separating nucleation from growth and producing monodisperse nanoparticles where particles with a 10 nm diameter are considered to be large. We are interested, however, in producing alloy nanoparticles that are large enough to evolve porosity, potentially requiring diameters as large as 20–30 nm. This requires adjustment of the kinetics of nucleation and growth during chemical synthesis, and we can gain some insight into how this may be approached from the chemical reduction mechanisms reported in the literature.

Mechanistic studies of monodisperse nanocrystal formation in solution commonly cite the LaMer mechanism[61] to describe the kinetic and thermodynamic processes associated with nanocrystal nucleation and growth. The LaMer mechanism states that homogeneous nucleation can only occur in supersaturated solutions, in which case nucleation proceeds rapidly over a short time period, so-called "burst nucleation", quickly depleting the monomer concentration in solution and preventing any further nucleation from occurring. This is followed by slow, diffusion-controlled growth resulting in monodisperse nanocrystals due to a sharp separation between the nucleation and the growth phases. There are limitations, however, that make the LaMer mechanism realistically appropriate only for very few systems. Finke et al.[62,63] challenged the LaMer mechanism because it cannot account for nuclei aggregation and Ostwald ripening which can greatly affect the monodispersity of the prepared nanocrystals. Also, diffusion of monomers to the growing particle's surface is not always the rate-determining step; incorporation of those monomers into the nanocrystal surface can be rate determining with direct dependence on the surface area of the nanocrystal. Finke et al.[62] proposed a mechanism in which nucleation occurs in a slow, continuous process rather than in a single burst, followed by an autocatalytic surface growth process whose rate depends on the particle surface area or number of active sites, i.e., growth is not diffusion limited as suggested in the LaMer mechanism.[61] In this case, growth is controlled and rate limited by incorporation of monomers into the surface of the nanocrystals, which is evidenced in formation of shape-controlled nanocrystals where uncapped or weakly capped surfaces grow at a higher rate than strongly capped surfaces, resulting in formation of nanorods/wires and other anisotropic shapes.[64−66] Autocatalytic growth also explains how monodispersity can be maintained with slow, continuous nucleation; smaller nanocrystals with higher surface energies will grow at a faster rate than larger, more thermodynamically stable particles in a process known as "focusing".[56,59] Finke's model highlights the importance of the interaction between precursor metal ions or metal ion-capping agent complexes and nanocrystals and the great effect that they can have on the kinetics of nucleation and growth. What is made clear in all of the experimental and theoretical studies of colloidal particle synthesis, regardless of the underlying mechanism, is that nucleation is the dominating factor determining final nanocrystal size, and strict experimental control of the nucleation process may be an ideal strategy for obtaining monodisperse colloidal particles in a wide range of diameters.

There continues to be a lack of an accurate, detailed, microscopic kinetic model describing nucleation and growth in colloidal nanocrystal synthesis, but we can gain some insight into how we may control these processes from a simplified assessment of classical nucleation theory. The rate of nuclei formation takes an Arrhenius form

$$\frac{\mathrm{d}N}{\mathrm{d}t} = A\exp\left[\frac{-\Delta G_{\mathrm{N}}}{k_{\mathrm{B}}T}\right] \quad (1)$$

$$\Delta G_{\mathrm{N}} = \frac{16\pi\gamma^3 V_{\mathrm{m}}^2}{3\,|\Delta\mu|^2} \quad (2)$$

$$\Delta\mu = RT\ln S \quad (3)$$

where N is the number of nuclei, A is a preexponential factor, k_B is Boltzmann's constant, and T is temperature. ΔG_N is the work required to form a critical nucleus for homogeneous nucleation given in eq 2, where γ is the surface free energy per unit area, V_m is the molar volume of the monomer in the crystal, $\Delta\mu$ is the difference in chemical potential of the metal species in the solid and as a monomer in solution, R is the gas constant, and S is a measure of the oversaturation ratio, i.e., the ratio of the actual and the equilibrium concentrations of monomer in solution. The nucleation rate is highly sensitive to the degree of oversaturation, and this can be adjusted by controlling the rate of formation of monomer or active species through changes in reaction temperature,[43] incubation time in the case of delayed nucleation,[58] and equilibrium concentration of the monomer by complexation with different capping agents.[56−60] While size control through adjustment of these experimental parameters is a good place to start, the complexity inherent in solvothermal synthesis of colloidal nanocrystals means that complete control is unlikely through simple parameter adjustments and will require some trial and error.

In this study, we report a chemical synthesis procedure, based on concepts developed within the solvothermal reduction process context, in which alloy nanoparticle size and composition may be controlled over a wide range while maintaining an adequate size distribution. This procedure was applied to the synthesis of Ni/Pt nanoparticles that were then electrochemically dealloyed to form nanoporous Ni/Pt nanoparticles. With reproducible control of both size and size distribution, we were able to study the effect of nanoparticle size on dealloying and porosity formation and show that there is a minimum particle diameter required for complete evolution of porosity. Further electrochemical characterization of the dealloying process led to insights into how to develop nanoporous Ni/Pt particles into electrocatalysts, and we demonstrate the remarkable activity of these high surface area, core−shell nanostructured catalysts for the cathodic ORR.

2. EXPERIMENTAL SECTION

2.1. Nanoparticle and Catalyst Synthesis. Alloy nanoparticles of Ni_xPt_{1-x} were synthesized through a solvothermal reduction process using organic precursor molecules in organic solvents. In a typical synthesis (~15 nm, $Ni_{75}Pt_{25}$ nanoparticles) 0.73 mmol of Ni(II) acetylacetonate ($Ni(acac)_2$) (Sigma Aldrich, 97%), 3 mmol of 1-adamantanecarboxylic acid (ACA) (Sigma Aldrich, 99%), 0.15 mmol of 1,2-tetradecandiol (TDD) (Sigma Aldrich, 90%), 0.10 mmol of borane-*tert*-butylamine (BtB) (Sigma Aldrich, 97%), 4 mL of oleylamine (Sigma Aldrich, 70%), and 10 mL of diphenyl ether (DPE) (Sigma Aldrich, ReagentPlus, 99%) were loaded into a four-neck flask and stirred at 500 rpm under a blanket of argon (Roberts Oxygen, Zero grade) in a glovebox (Labconco). The stirring solution was heated using a mantle (Optichem, Chemglass) at a rate of approximately 2 °C/min^{-1}. Once the solution reached 225 °C, 0.27 mmol of Pt(II) acetylacetonate ($Pt(acac)_2$) (Sigma Aldrich, 97%) dissolved in 3 mL of dichlorobenzene (DCB) (Sigma Aldrich, 99%) at 100 °C was quickly injected into the stirring solution. After a slight decrease, the temperature quickly rose back to 225 °C where nucleation occurred, as evidenced by darkening of the solution. After holding the solution for 60 min at 225 °C, the solution was allowed to cool to room temperature under an argon blanket. The cooled solution was then dispersed in a 50/50 vol/vol % mixture of hexane (Fisher Scientific, ACS grade) and ethanol (Pharmco-Aaper, 200 proof) and centrifuged (Thermo Scientific, CL2) to separate out the particles. After removing the effluent, the particles were again washed in the hexane/ethanol mixture and then centrifuged out of solution. This was repeated four times in order to remove the bulk of the organic capping agents. The cleaned particles were then loaded onto a carbon support (XC-72R, Cabot) through a colloidal deposition process. Briefly, ~60 mg of particles was dispersed in 50 mL of chloroform (Fisher Scientific, ACS grade) with 20 μL of oleylamine to aid in the dispersion, while in a separate vessel an appropriate amount of carbon support (in this study we used 30 wt % particles on carbon) was dispersed in chloroform. Each solution was sonicated separately for 45 min, being careful to ensure that the solutions remained at or below room temperature by placing ice in the sonicator bath. The nanoparticle solution was then added dropwise to the carbon solution, and they were sonicated together for a further 45 min. The loaded catalyst was then transferred to hexane and stirred overnight. The as-made and supported catalysts were homogenized in a tube furnace (Lindberg) under H_2/Ar 5%/95% (Roberts Oxygen, Zero grade) at 400 °C.

2.2. Electrochemical Measurements. Homogenized nanoparticle catalysts were dealloyed, electrochemically characterized, and assessed for oxygen reduction activity in a three-electrode cell with a Pt mesh (Alfa Aesar) counter electrode and a Hg/Hg_2SO_4 (MSE) reference electrode. The reference electrode was calibrated against a hydrogen electrode fabricated according to the specifications in ref 67. Nitrogen was bubbled through a 0.1 M $HClO_4$ (70%, Sigma Aldrich, redistilled 99.999%) solution for at least 30 min in order to remove any trace dissolved oxygen. Both the hydrogen electrode and Hg/Hg_2SO_4 were placed in the solution, and the voltage between them was measured to be 0.722 V. The Hg/Hg_2SO_4 offset from the hydrogen reference potential was further confirmed by multiple comparisons to other reference electrodes, as well as to the positions of characteristic peaks for H_{UPD} and Pt oxidation/reduction found in the literature.[5−8] Prior to any electrochemical experiments, all glassware was cleaned by soaking in a solution of concentrated H_2SO_4 (J. T. Baker, ACS grade) and Nochromix cleaner (Godax Laboratories, Inc.) for at least 8 h followed by rinsing in Millipore water. All solutions were made using Millipore (Milli-Q Synthesis A10) water with a resistivity greater than 18.2 MΩ cm.

Supported, annealed catalysts were dispersed in a 4:1 H_2O:IPA volume solution at a concentration of 3 $mg_{catalyst}$ mL^{-1}; 0.4 μL $mg_{catalyst}^{-1}$ of a 5 wt % Nafion/IPA solution was added to the catalyst ink to aid in dispersion and adhesion of the catalyst particles to the glassy carbon (GC) disk (5 mm diameter, 0.196 cm^2, Pine Instruments). Prior to loading with catalyst, the GC disk was polished to a mirror finish using progressively finer diamond paste down to 0.1 μm (Buehler) and sonicated in Millipore water to remove contaminants. The appropriate volume of catalyst ink to achieve a loading of 12 μg_{Pt} cm^{-2} was pipetted onto the GC disk and dried under a flow of argon to form a uniform layer. Catalytic activity is directly dependent on the quality of the catalyst layer on the disk.[68,69] Dealloying of catalysts was accomplished in N_2-purged (Roberts Oxygen, Zero grade) 0.1 M H_2SO_4 by cycling the potential between 0.05 and 1.2 V vs RHE (Gamry 750 mA potentiostat) at 250 mV s^{-1} for at least 50 cycles or more if the cyclic voltammetry (CV) curve had not yet reached a steady state; all quantitative CVs used a sweep rate of 50 mV s^{-1}. The ECSA of the dealloyed catalysts was found through integration of the current in the hydrogen underpotential deposition (H_{UPD}) region of the CVs, subtracting out the double-layer charging, and assuming 210 μC cm^{-2}. After the catalyst was fully dealloyed, it was rinsed thoroughly in Millipore water and transferred to O_2 (Roberts Oxygen, Research grade) saturated 0.1 M $HClO_4$ at 25 °C for ORR activity measurements. Using a Pine Instruments rotator (AFMSRCE), the GC disk was rotated at a desired rpm while running linear sweep voltammetry from 0.1 to 1.1 V vs RHE at 5 and 20 mV s^{-1}. Currents were corrected for ohmic *iR* drop through the process described in ref 70.

2.3. Microscopy Characterization. The microstructure of the as-made and dealloyed nanoparticles was visually characterized using both scanning electron microscopy (SEM) and transmission electron microscopy (TEM). SEM was performed on a JEOL JSM-6700F Field Emission Scanning Electron Microscope equipped with an EDAX microanalysis system. TEM was performed on a 300 kV, field-emission Philips CM300-FEG TEM at the Electron Microscopy Center at Johns Hopkins University. An EDAX X-ray microanalysis system on the TEM was used to measure Ni and Pt fractions in the nanoparticle samples.

3. RESULTS AND DISCUSSION

3.1. Nanoparticle Synthesis. Figure 1 is a series of scanning electron micrographs (SEM) of $Ni_{75}Pt_{25}$ alloy nanoparticles (composition chosen based on results in ref 33) in which particle diameter was controlled by altering the concentration of ACA capping agent in solution. In each case, $Pt(acac)_2$ dissolved in DCB was injected just below the temperature at which nucleation is known to take place. From the SEMs it is clear that increasing amounts of ACA resulted in an increase in the average size of the Ni/Pt alloy nanoparticles. Although a second capping agent, oleylamine, was present in solution with the ACA, it had a negligible effect on nucleation and was used to aid in the control of the final size distribution and particle shape.[71−73] Growth with increasing ACA concentration is a result of an adjustment of the nucleation kinetics. For single-component nanoparticles,[56,58,59] ACA has been found to form a stable complex with the monomer delaying and impeding nucleation, producing a smaller number of nuclei with increasing ACA concentration which then grow into larger diameter particles. In our case, the simultaneous reduction of two elemental species, Ni and Pt, can complicate the process. How can we simultaneously adjust the nucleation and reduction kinetics for two metal ions that have significantly different reduction potentials? Fortunately, it is very difficult to

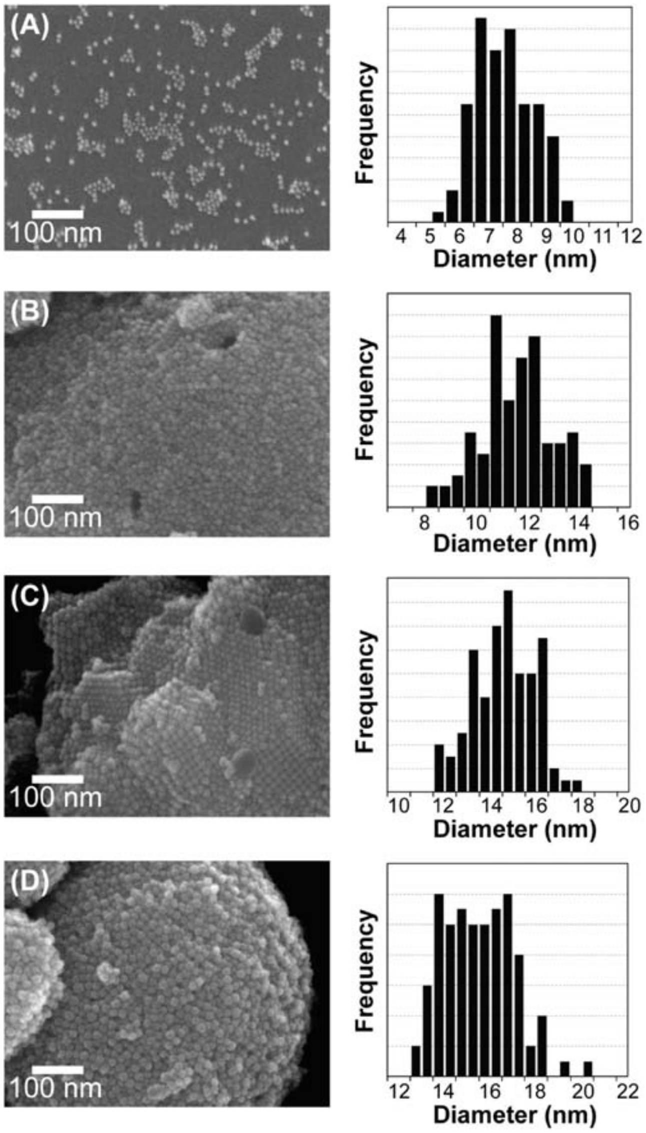

Figure 1. Scanning electron micrographs (SEM) of $Ni_{75}Pt_{25}$ nanoparticles synthesized using the procedure outlined in section 2.1 with ACA concentrations of (A) 0.1, (B) 0.2, (C) 0.3, and (D) 0.5 M. For each sample, Pt precursor was injected at a temperature just below that at which particles are known to nucleate at those ACA concentrations, Table 1, resulting in a very short induction time. Size distribution charts for each sample are included to the right of each SEM.

homogeneously nucleate Ni under the current experimental conditions. With 3 mmol of ACA in 10 mL of DPE solvent (0.3 M), a solution containing just $Ni(acac)_2$ would not begin to darken, indicating initiation of Ni nucleation, until a temperature of ~260 °C was reached. On the other hand, that same solution replacing $Ni(acac)_2$ with $Pt(acac)_2$ began to darken at ~215 °C, while a solution with both $Ni(acac)_2$ and $Pt(acac)_2$, maintaining the same total molar metal loading, began to darken at ~225 °C. Ni will not reduce on its own until 260 °C, but Ni/Pt alloy nanoparticles were easily formed at 225 °C. These observations suggest that the reduction of Ni was induced by Pt, an observation in agreement with the autocatalytic growth mechanism of Finke,[62,63] where reduction of monomer species is catalyzed by the growing metal surface. This also agrees with a reduction mechanism described by Li et al.,[74,75] whereby reduction of non-noble metal ions is induced through electron transfer from noble metal atoms on the surface of growing nanocrystals aided by the noble metal's high electron affinity. Therefore, nucleation was initiated and dominated by the reduction of Pt and, as will be shown later, resulted in alloy nanoparticles composed of a Pt-rich core and a Ni-rich shell. We can infer then that particle size variance is a consequence of the nucleation kinetics of Pt alone with Ni acting as a spectator.

The ACA capping agent can affect the final size of alloy nanoparticles in several ways: (1) if the ACA is bound relatively weakly with the surface metal atoms, it may reversibly coordinate with the metal allowing further growth through reduction of ionic species on the particle surface;[76] (2) the bulky adamantyl groups of the ACA molecules, through steric hindrance, may leave free sites on the surface that are active for further growth;[71] (3) ACA can form a complex with the monomer which will adjust the nucleation process.[56−60] While all valid, the most influential pathway for particle growth through ACA addition is likely the third, where formation of a monomer−ACA complex effectively increases the equilibrium concentration of the monomer in solution resulting in a decrease in the monomer oversaturation, S. From eq 3 we can see that a decrease in S will also lower $\Delta\mu$, increasing ΔG_N and decreasing the nucleation rate. A lower nucleation rate will allow for growth on a smaller number of seed nuclei and yield larger particles. In Table 1 the inhibition of nucleation is evidenced by the increase in temperature required to initiate nucleation with increased ACA concentration. However, there is an upper limit to this trend. Beyond ACA concentrations of 0.3 M there was no further increase in the nucleation temperature or particle size as shown in Table 1 and Figure 1. It is possible that the entire amount of Pt in solution was fully complexed at 0.3 M ACA, and adding any additional ACA resulted in no further change in the nucleation rate. Another possibility is that the higher temperatures required to initiate nucleation at ACA concentrations above 0.3 M destabilize the monomer−capping agent complex in solution, lowering the equilibrium concentration and negating the effect of the increased amount of ACA.[59]

Table 1. Particle Nucleation Temperatures As a Function of ACA Concentration and Pt Precursor Injection Temperature and the Resulting $Ni_{75}Pt_{25}$ Alloy Particle Sizes

ACA concentration (M)	Pt injection temp. (°C)	reduction temp. (°C)	mean particle diameter (nm)
0.1	202	203	7.6 ± 0.99
0.2	209	212	11.6 ± 1.44
0.3	223	225	14.6 ± 1.34
0.5	224	226	15.5 ± 1.52
0.5	200	226	20.0 ± 2.35

Injection of metal salt precursors into high-temperature solvents is designed to induce burst nucleation that is quickly quenched in order to effectively separate nucleation from growth. However, it has been observed that injection of precursors does not often lead to immediate supersaturation and nucleation.[56,58] Rather, injection causes a dip in temperature of the solvent followed by slow heating during which the metal salt is decomposed, increasing the monomer concentration until nucleation can occur. This process of delayed nucleation is controlled by formation of intermediates, either by decomposition of the precursor salts to form "monomers" or through complexation of the metal ions with organic capping agents which are then transformed into an "active species". Delayed nucleation can be exploited to vary nanocrystal size by varying the length of this "incubation" period, time between precursor injection and initiation of nucleation, and consequently the rate at which the monomer/active species concentration increases through adjustment of the heating rate of the solution after injection. For short incubation times, a fast increase in monomer concentration occurs due to a high heating rate, saturation of the solution is quickly reached, and particles nucleate at a relatively high rate, producing a large number of seeds where the small amount of remaining monomer in solution grows those seeds into small particles. On the other hand, longer induction times achieved through injection of metal precursors at lower temperature or use of slower heating rates have been shown to produce larger particles due to slower nucleation.[58,77−79] Growth of Ni/Pt alloy particles with diameters greater than those in Figure 1C and 1D can be achieved by varying the temperature at which the Pt precursor was injected into the solution and the rate at which the temperature was increased from injection to the desired nucleation and growth temperature of the solution. In Figures 1D and 2A, Pt was injected at a temperature just below the temperature required to initiate nucleation (225 °C) for a solution with 0.5 M ACA, allowing for a very short induction period while the solution temperature recovered from the slight drop due to the injection. Figure 2B is a SEM of a sample in which the Pt precursor was injected at 200 °C; in this case, the induction period was much longer as the temperature slowly rose to that at which nucleation occurred. The lower injection temperature and slower heating rate produced monomers at a lower rate, and therefore, the solution reached the proper supersaturation over a longer period of time. This not only decreased the rate of nucleation but also increased its duration before growth took over, resulting in a slightly broader size distribution as seen in Figure 2B; however, focusing[56,59] likely occurring during growth helped to maintain an adequate size distribution. To summarize this section, use of ACA to form a precursor−capping agent complex in combination with careful tailoring of the incubation period, schematically represented in Figure 3, has allowed precise and predictable control of alloy particle size up to diameters that have been notoriously difficult to reach with Pt alloys without compromising on the quality of the size distribution.

3.2. Dealloying and Porosity Evolution in Nanoparticles.

With the ability to reliably and reproducibly control size and composition for the Ni/Pt alloy nanoparticles, we now

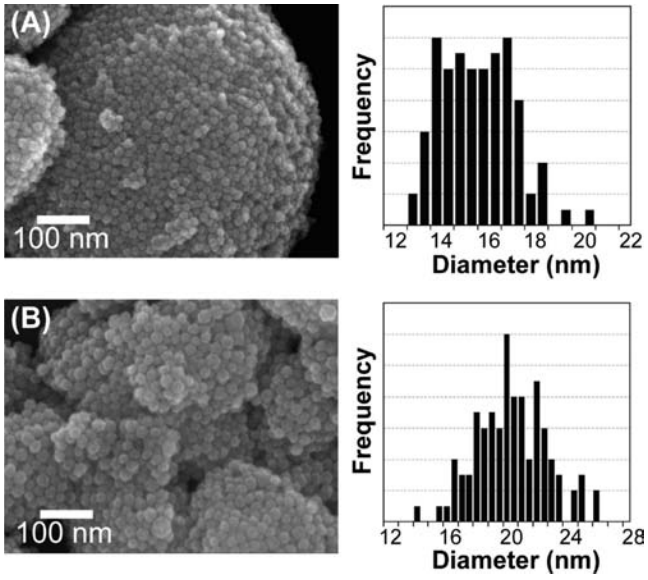

Figure 2. SEMs of $Ni_{75}Pt_{25}$ nanoparticles synthesized with an ACA concentration of 0.5 M. Pt precursor injected at (A) 225 °C with rapid heating rate to nucleation temperature (short induction period) and (B) 200 °C with slow heating rate to nucleation temperature (long induction period).

discuss the effect that initial alloy particle size has on both dealloying and porosity formation as well as electrocatalytic activity. Figure 4 contains as-made and postmortem TEMs of alloy nanoparticles that have been supported on carbon, annealed, and dealloyed by quickly cycling the potential between 0 and 1.2 V vs RHE in 0.1 M H_2SO_4. Table 2 contains the resulting Pt ECSA and residual Ni fraction for each particle after dealloying. It is evident that there is a minimum nanoparticle diameter for which porosity may form. For particles with an initial diameter of 8 nm (Figure 4A and 4B), porosity did not evolve; they were simply etched down to smaller core−shell nanoparticles. The 12 nm nanoparticles (Figure 4C and 4D) appear to be just below the size required for formation of uniform porosity where some particles have a tenuous misshapen porous structure, others formed hollow particles, and still others remained solid. On the other hand, dealloying of both the 15 nm (Figure 4E and 4F) and 20 nm (Figure 4G and 4H) diameter particles resulted in characteristic and fully formed porosity where all of the nanoparticles within the supported catalyst samples evolved an equivalent porosity, and after dealloying there were no solid particles remaining. The visible lattice fringes in the HRTEM of the 15 nm np-NiPt nanoparticle in Figure 5 show that the porous particles are single crystals and the lighter regions of the particle are in fact voids rather than some compositional inhomogeneity. The series of TEMs in Figure 4 suggest that the minimum initial nanoparticle diameter for dealloying to result in formation of porosity under standard dealloying conditions lies somewhere between 12 and 15 nm for the Ni/Pt system.

For single-component metal nanoparticles, the electrochemical potential required for dissolution of the metal species is greatly affected by the high radius of curvature of the surface and decreases with radius, *r*, of the nanoparticle due to a Gibbs−Thomson effect.[80,81] In contrast, kinetic Monte Carlo (KMC) simulations performed by our group[82] predict that the electrochemical potential required to initiate *porosity* formation in metal alloy nanoparticles, E_{crit}, increases with $1/r$. In other words, higher potentials are required to drive formation of porosity in smaller diameter particles, in contrast to simply enriching the surface layer by dealloying the outermost surface. Under potential, the surface of a nanoparticle is quickly enriched in and passivated by the more-noble component as the less-noble metal is etched from low-coordinated sites on the particle's surface. After some time under potential, surface fluctuations may cause pits to appear in the passivation layer and at sufficient electrochemical potential and dissolution rate those fluctuations may be adequately long lived to allow exposure of an underlying percolation network of the less noble-component, propagating dissolution and evolving porosity. These fluctuations increase in frequency but decrease in duration as the particle diameter decreases due to the increased

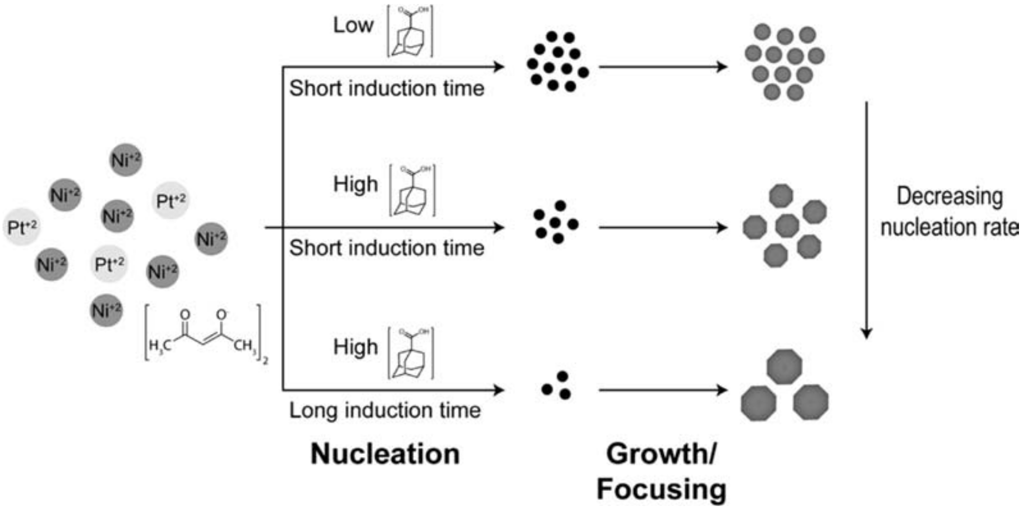

Figure 3. Schematic diagram demonstrating our procedure for size control of Ni/Pt alloy nanoparticles. At low concentrations of the ACA capping agent and short induction times (solution temperature rapidly reaches nucleation temperature after Pt precursor injection) the nucleation rate is high, producing a large number of seeds that grow to small alloy nanoparticles. In contrast, at high ACA concentrations and long induction times the nucleation rate is comparatively slow, producing a smaller number of seeds with a large amount of residual monomer with which to grow those seeds into larger particles.

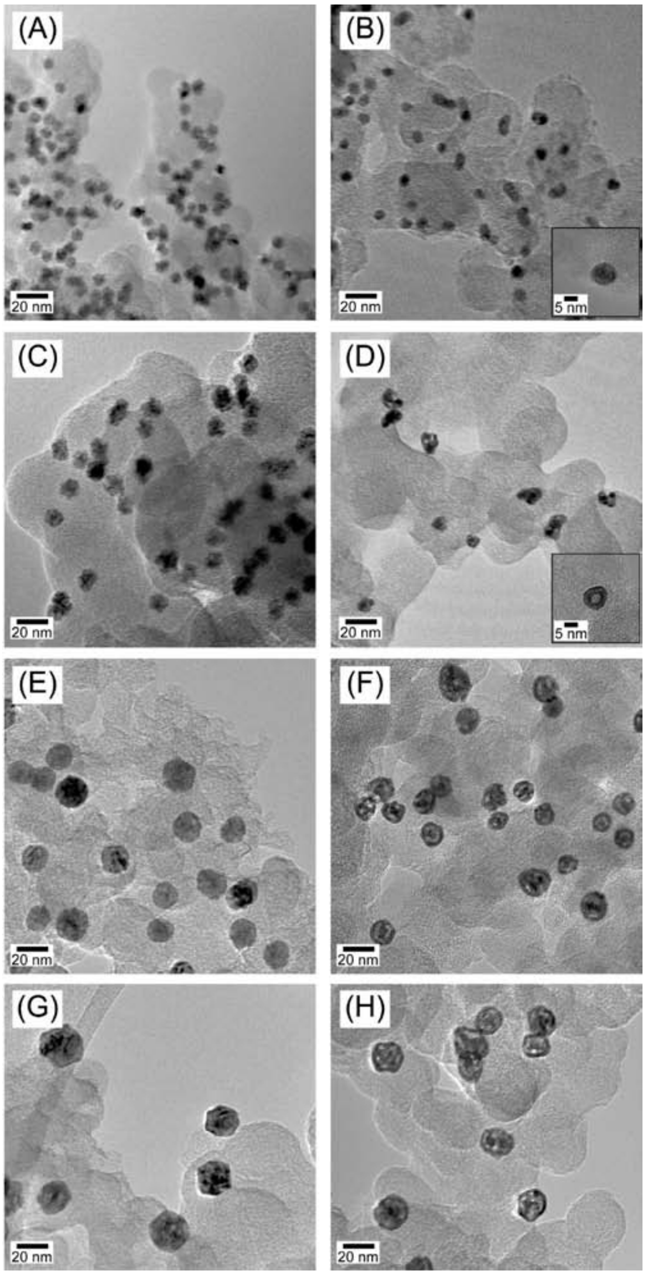

Figure 4. Transmission electron micrographs (TEMs) of carbon-supported $Ni_{75}Pt_{25}$ as-made ((A) 8, (C) 12, (E) 15, and (G) 20 nm) and annealed (400 °C, H_2/Ar)/dealloyed (potential cycling from 0 to 1.2 V vs RHE in deaerated 0.1 M H_2SO_4 at 25 °C) ((B) 8, (D) 12, (F) 15, and (H) 20 nm).

Table 2. Electrochemically Active Pt Surface Area (ECSA) and Residual Ni Fraction for Carbon-Supported, -Annealed, and -Dealloyed $Ni_{75}Pt_{25}$ nanoparticles

NiPt nanoparticle diameter (nm)	Pt ECSA (m^2 g_{Pt}^{-1})	residual Ni (atom %)
8	47.9 ± 3.0	27
12	37.8 ± 4.7	porous, 15; solid, 38
15	41 ± 0.5	27
20	38.8 ± 1.4	33

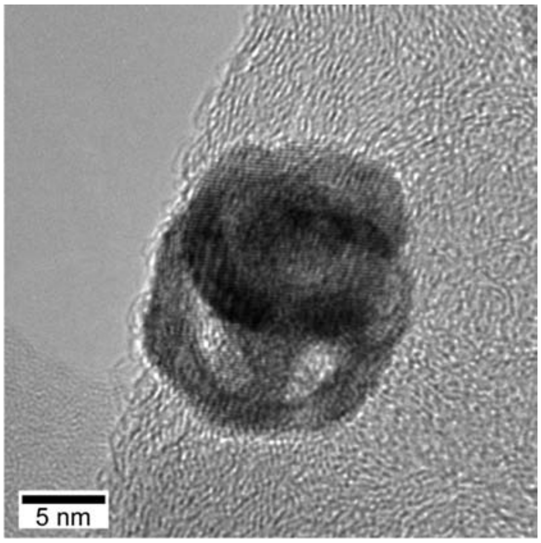

Figure 5. High-resolution transmission electron micrograph (HRTEM) of 15 nm np-NiPt nanoparticle.

surface mobility associated with Gibbs−Thomson effects.[80] The increase in E_{crit} with particle size is not associated with an increase in the dissolution potential for the less-noble component; in fact, the surface of the smaller diameter particles is enriched in the more-noble component at a faster rate due to the higher density of low-coordination sites such as steps and kinks from which the less-noble component is easily etched. Rather, the high step density present on the surface of small diameter nanoparticles contributes to the mobility of the more-noble species, leading to fast passivation. This means that it may require unrealistically high potentials in order to evolve porosity in smaller nanoparticles, below 15 nm. We can see this effect in the postdealloying Pt ECSA and residual Ni fractions for each size nanoparticle, listed in Table 2. For both the 15 and the 20 nm nanoparticles, porosity evolved and they both had similar ECSA and residual Ni, and these values agree well with the values we reported for planar, bulk np-NiPt.[33] However, for the 12 nm particles, the mix of porous and nonporous particles suggests the mobility of the surface Pt was too high for a certain fraction of the particles and any fluctuations in the surface passivating layer after depletion in Ni are not sufficiently long lived to yield porosity, the net result being a mix of potentially porous and nonporous particles with a core−shell composition. The residual Ni fraction of the nonporous particles is higher than that for the porous particles because the fast surface passivation prevented a large fraction of Ni from being exposed to electrolyte. The smaller 8 nm particles also quickly passivated after depletion of surface Ni, likely at an even faster rate than for the 12 nm nanoparticles, but because the surface area to volume ratio is higher for the smaller particles, a larger fraction of Ni was etched from the surface, resulting in a lower residual Ni content.

Figure 6 contains sequential CVs recorded as dealloying progressed for the annealed (400 °C, 1 h) 15 nm $Ni_{75}Pt_{25}$ alloy nanoparticles during which porosity evolved. We dealloyed the nanoparticles through electrochemical potential cycling to initiate roughening of the surface and "artificially" increase the magnitude, lifetime, and frequency of fluctuations in the surface passivation layer to aid in formation of porosity. Just slightly positive of the H_{UPD} region, as the potential was swept anodically, there is a very slight bump at ∼0.4 V vs RHE in the curve of the first cycle that can be attributed to dissolution of Ni from the surface of the nanoparticle, primarily from low-coordinated sites.[24] The magnitude of this current is relatively

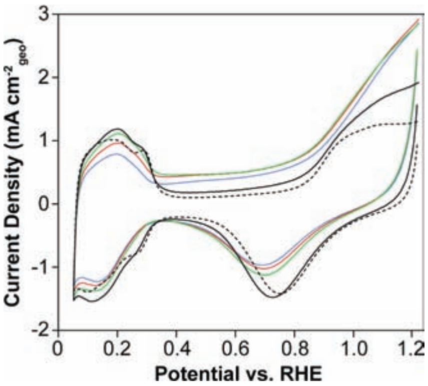

Figure 6. Sequential CVs recorded during dealloying of annealed 15 nm $Ni_{75}Pt_{25}$ nanoparticles in deaerated 0.1 M H_2SO_4 at 25 °C and a sweep rate of 250 mV s^{-1}. Curves represent 1st cycle (blue), 2nd cycle (red), 3rd cycle (green), 10th cycle (solid black), and 40th cycle (dashed black).

low because there was an even, homogeneous dispersion of Ni and Pt within the nanoparticles, preventing copious dissolution of Ni during the initial potential cycles. In the subsequent potential cycles, as the surface roughened, dealloying progressed as indicated by the growth of both the current due to H_{UPD} and the nonfaradaic current due to double-layer charging. As dealloying continued to the point where the etch front had progressed to the center of the nanoparticles and porosity became fully formed, the current in the double-layer charging region began to drop due to cessation of Ni dissolution as the surface passivated with Pt and also due to electrochemical annealing of the porous structure's surface. As a consequence of the dealloying process, the surface of nanoporous metals contains a high density of low-coordinated sites, i.e., the surfaces are very rough. Continually cycling the potential after porosity has fully formed induces motion of the passivating more-noble species which, driven by capillary forces, will tend to smoothen out atomic-scale roughness of the surface. This process of electrochemical annealing is shown not only through a narrowing of the double-layer charging current but also as a dip in the H_{UPD} currents and a leveling off and refining of the Pt surface oxidation current at higher potentials in the anodic current sweep as the surface "smoothened" (see dashed line in Figure 6). Initially, the H_{UPD} region of the CV contained one broad peak, but through continued cycling two distinct peaks appeared as the population and size of the most stable low-index facets increased, which happens to be another consequence of electrochemical annealing. There was also a shift in the surface oxide reduction peak to more positive potentials as the surface became enriched in Pt. This picture of dealloying portrayed through the progression of the CV curve signatures agrees well with the mechanism for dealloying and porosity evolution in nanoparticles elucidated through KMC simulations[82] where the important processes are (1) depletion of Ni from the low-coordinated sites on the surface of the nanoparticles, (2) roughening of the surface passivation layer to expose underlying percolations of the less noble component, (3) progression of the etch front through the particle, and (4) capillarity-driven smoothening of the nanostructure surface.

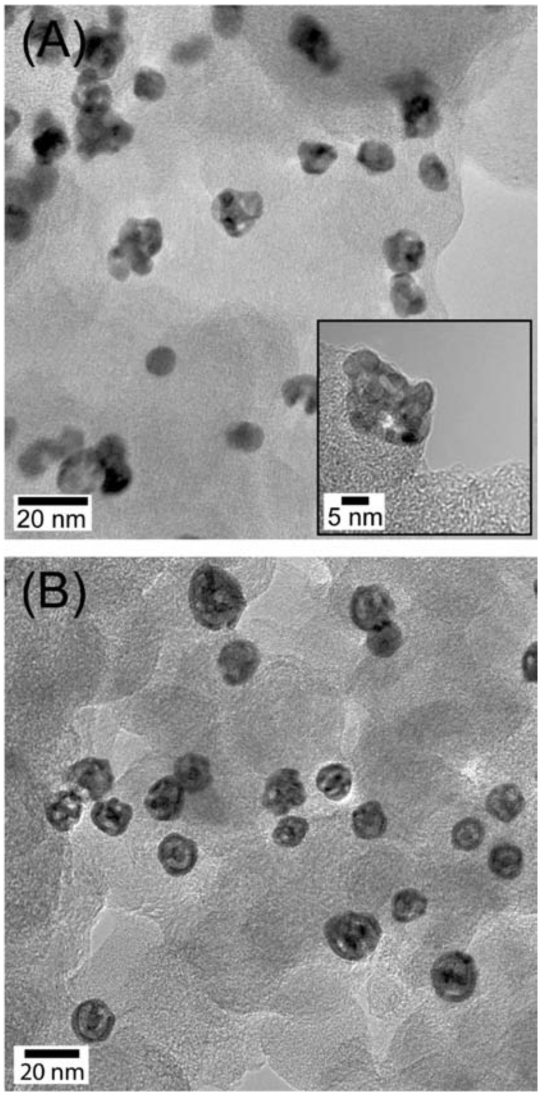

Figure 7. TEMs of (A) as-made and (B) annealed (400 °C, 1 h, H_2/Ar) 15 nm $Ni_{75}Pt_{25}$ nanoparticles postdealloying by cycling the potential in deaerated 0.1 M H_2SO_4 at 25 °C.

The importance of annealing/homogenizing the $Ni_{75}Pt_{25}$ nanoparticles prior to dealloying is shown in Figure 7, which contrasts TEMs of dealloyed as-made and annealed nanoparticles. While the dealloyed as-made nanoparticles were in fact porous, their final structure was much less symmetrical than the annealed particles (inset in Figure 7A); also, careful examination of Figure 7A finds that there were some particles that were not porous and simply etched down to smaller solid nanoparticles. Annealing is useful for removing residual organic capping ligands from the particle surface and ensuring that each particle has a homogeneous dispersion of the alloying components. The as-made alloy nanoparticles, therefore, do not have a homogeneous composition, and Ni-rich areas of the particles were more easily etched. As mentioned earlier, Ni reduction is induced through autocatalytic growth on the surface of preformed Pt seeds; therefore, there is likely a slight gradient in composition within the as-made nanoparticles where the interior tends toward a Pt-rich composition and the exterior of the nanoparticles tends toward a Ni-rich composition. This hypothesis is corroborated through careful inspection of the dealloying CV curves (Figure 8). Comparing Figure 8 to Figure 6 it is evident that the as-made particles had a higher population of Ni near the surface prior to dealloying as the initial Ni dissolution peaks are much larger in comparison to that for the homogenized particles. As a direct consequence

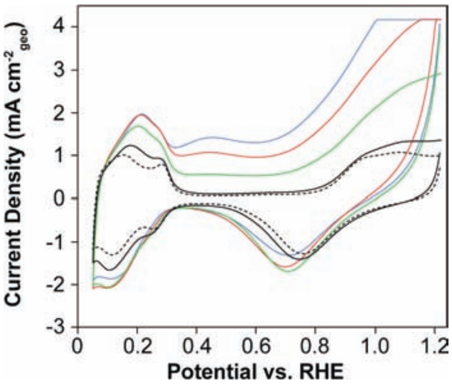

Figure 8. Sequential CVs recorded during dealloying of as-made (unannealed) 15 nm $Ni_{75}Pt_{25}$ nanoparticles in deaerated 0.1 M H_2SO_4 at 25 °C and a sweep rate of 250 mV s^{-1}. Curves represent 1st cycle (blue), 2nd cycle (red), 3rd cycle (green), 10th cycle (solid black), and 40th cycle (dashed black).

of this compositional inhomogeneity, a certain population of the nanoparticles failed to form porosity and the residual Ni composition droped to 13 atom % compared to 27 atom % for the annealed sample. The failure to form complete nanoporosity throughout the sample resulted in a lower ECSA, 34 $m^2\ g_{Pt}^{-1}$ (Figure 9A), which combined with the lower residual Ni content negatively affected the activity of the catalyst (Figure 9B).

3.3. Electrochemical Characterization and ORR Activity of Nanoporous Nanoparticles.

Figure 10A contains cyclic voltammograms (CVs) of 15 nm np-NiPt nanoparticles and 30 wt % Pt/C on a GC disk at a loading of 12 $\mu g_{Pt}\ cm^{-2}$ in deaerated 0.1 M $HClO_4$. The ECSA for Pt/C was found to be 60 $m^2\ g_{Pt}^{-1}$, while that for the np-NiPt nanoparticles was found to be 41 $m^2\ g_{Pt}^{-1}$, which agrees well with the value found for a planar np-NiPt disk.[33] The CV for the np-NiPt nanoparticles is characterized by broad H_{UPD} peaks due to their polyfaceted, core−shell structure common to nanoporous metals.[33] The positive shift in the onset potential for Pt oxide formation compared to Pt/C indicates that the surface Pt is less oxophilic, which is a direct result of the shift in the d-band center induced by the presence of Ni in the catalyst and is a common feature of Pt/transition metal alloy catalysts.[6,14,16] The ORR activity for the 15 nm np-NiPt nanoparticles was measured vs Pt/C as shown in Figure 10B along with the Tafel curves in the inset. The final data was corrected for *iR* losses as in ref 70 along with subtraction of all nonfaradaic currents. At 0.9 V, the specific activity for the 15 nm np-NiPt nanoparticles was found to be 2.98 ± 0.12 mA $cm^{-2}{}_{Pt}$ and the mass activity was found to be 1.16 ± 0.035 mA μg_{Pt}^{-1} whereas the numbers for 30 wt % Pt/C were 0.5 ± 0.006 mA $cm^{-2}{}_{Pt}$ and 0.298 ± 0.003 mA μg_{Pt}^{-1}, respectively. Care must be taken, however, when using these numbers to make direct comparisons to other catalysts reported in the literature as experimental conditions can have a dramatic impact on measured activity. Table 3 contains ORR results for both 15 nm np-NiPt nanoparticles and Pt/C recorded at sweep rates of 5 and 20 mV s^{-1} where the values for the 5 mV s^{-1} sweep rate were considerably lower than those at 20 mV s^{-1}. This drop in measured activity may be directly associated with the slower sweep rate, which allows for a longer residence time at low overpotentials where intermediate oxide species may poison the catalytic surface. Therefore, a more accurate

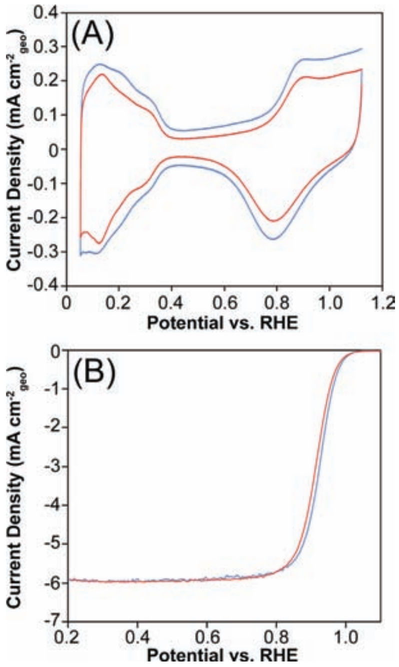

Figure 9. (A) CVs for annealed (blue) and unannealed (red) dealloyed 15 nm $Ni_{75}Pt_{25}$ nanoparticles in deaerated 0.1 M $HClO_4$ at 25 °C measured with a sweep rate of 50 mV s^{-1} and an electrode rotation rate of 1600 rpm. (B) ORR curves for annealed (blue) and unannealed (red) dealloyed 15 nm $Ni_{75}Pt_{25}$ nanoparticles in O_2-saturated 0.1 M $HClO_4$ at 25 °C measured with a sweep rate of 20 mV s^{-1}.

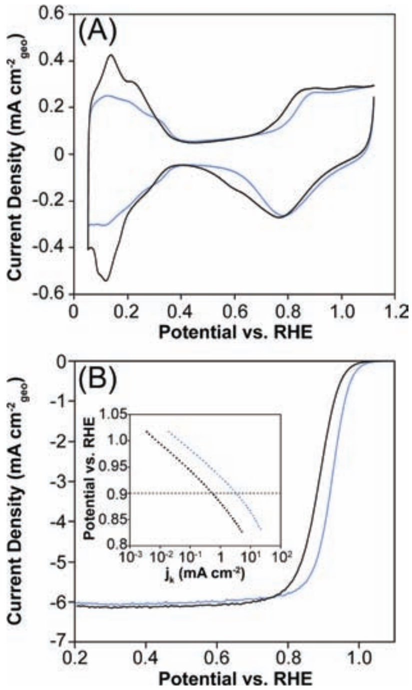

Figure 10. (A) CVs for Pt/C (30 wt.%, ETEK) (black line) and annealed/dealloyed 15 nm np-NiPt nanoparticles supported on carbon (blue line) in deaerated 0.1 M $HClO_4$ at 25 °C and measured with a sweep rate of 50 mV s^{-1}. (B) ORR curves for Pt/C (black line) and annealed/dealloyed 15 nm np-NiPt nanoparticles (blue line) measured in O_2-saturated 0.1 M $HClO_4$ at 25 °C, 20 mV s^{-1} sweep rate, and rotation rate of 1600 rpm. (Inset in B) Tafel plots for Pt/C and 15 nm np-NiPt. Loading on GC disk was 12 $\mu g_{Pt}\ cm^{-2}$.

Table 3. *iR*-Free ORR Kinetic Parameters As a Function of Sweep Rate[a]

	5 mV s^{-1}		20 mV s^{-1}		
catalyst	specific activity (mA $cm^{-2}{}_{Pt}$)	mass activity (mA $\mu g_{Pt}{}^{-1}$)	specific activity (mA $cm^{-2}{}_{Pt}$)	mass activity (mA $\mu g_{Pt}{}^{-1}$)	Pt ECSA (m^2 $g_{Pt}{}^{-1}$)
Pt/C (30 wt % ETEK)	0.334 ± 0.005	0.199 ± 0.003	0.5 ± 0.006	0.298 ± 0.003	60 ± 1.9
15 nm np-NiPt	2.25 ± 0.02	0.895 ± 0.03	2.98 ± 0.12	1.16 ± 0.04	41 ± 0.5

[a] ORR curves recorded in O_2-saturated 0.1 M $HClO_4$ at 25 °C and a rotation rate of 1600 rpm. Each data point is an average of at least three independent experiments.

representation of the ORR data is achieved through direct comparison of catalyst activities measured in the same experimental setup with identical experimental parameters. By doing this we find that the 15 nm np-NiPt nanoparticles are approximately six times more active, in terms of specific activity, than 30 wt % Pt/C independent of sweep rate. In this study we calculated our specific activities by normalizing the kinetic current by the H_{UPD} surface area as is common among other assessments of Pt alloy catalyst activity in the literature.[21,24,26,83] However, we are aware of the potential underestimation of the ECSA by using the H_{UPD} surface area for Pt-skin or Pt-skeleton, Ni/Pt alloy catalysts; for such materials, CO oxidation has been found to give a more accurate value.[7,14] This being the case, a more accurate comparison is made with the mass activities, where we find that the 15 nm np-NiPt nanoparticles have an activity on a per mass of Pt basis approximately four times that of 30 wt % Pt/C.

Figure 11 summarizes the activities for all of the dealloyed nanoparticles in comparison to 30 wt % Pt/C, commercial catalyst, measured in the same setup under the same experimental conditions (actual activity numbers are listed in Table 4). Also shown on this chart are the 2015 DOE targets[84] for both specific and mass activity, represented as data points on both axes. Each activity data point is an average of at least three separate measurements on at least three different samples where the error in measurement is under 5%. The activities for each of the dealloyed catalysts are well above Pt/C, presumably due to residual Ni within the interior of the dealloyed nanoparticles and for the two largest particle samples the presence of porosity. The trend in activities among the different dealloyed samples agrees well with the postmortem TEMs. Both the 15 and the 20 nm nanoparticles evolved porosity during dealloying, and both have nearly the same specific and mass activities, the highest among all of the dealloyed particle sizes. Moving from the 15 nm particles to the 12 nm particles, there is a significant drop in activity; this may be associated with the loss of fully formed porosity. The 12 nm particle samples are composed of a mixture of tenuously porous and relatively large solid particles resulting in a low ECSA, a low amount of residual Ni in the "porous" particles, and consequently a low activity. The mass activity rises moving from the 12 nm particles to the 8 nm particles. The 8 nm particles are too small to evolve porosity and simply etch down to smaller, Pt-rich nanoparticles, but due to their smaller size they have a higher ECSA. The activities of the solid, dealloyed 8 nm nanoparticles determined in this study agree well with values for similar Ni/Pt nanoparticle catalysts reported in the literature.[21,24,26]

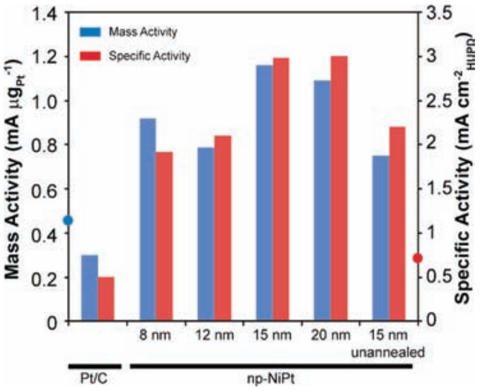

Figure 11. Bar chart comparing mass (blue bars) and specific (red bars) activities of dealloyed Ni/Pt nanoparticles to that of Pt/C (30 wt %, ETEK). Blue and red dots on the mass and specific activity axes, respectively, represent the *iR*-free 2015 DOE targets.[84] All kinetic numbers were extracted from ORR curves measured in O_2-saturated 0.1 M $HClO_4$ at 25 °C, 20 mV s^{-1}, and a rotation rate of 1600 rpm with a GC disk loading of 12 μg_{Pt} cm^{-2}. Each data point is an average of at least three individual samples where the deviation is below 5%.

Table 4. *iR*-Free ORR Kinetic Activity Parameters for Each Dealloyed Ni/Pt Catalyst and 30 wt % Pt/C[a]

NiPt nanocatalyst	specific activity (mA $cm^{-2}{}_{Pt}$)	mass activity (mA $ug_{Pt}{}^{-1}$)	Pt ECSA (m^2 $g_{Pt}{}^{-1}$)
8 nm	1.92 ± 0.16	0.917 ± 0.063	47.9 ± 3.0
12 nm	2.10 ± 0.20	0.785 ± 0.037	37.8 ± 4.7
15 nm	2.98 ± 0.12	1.16 ± 0.04	41 ± 0.5
20 nm	3.0 ± 0.08	1.09 ± 0.035	38.8 ± 1.4
Pt/C (30 wt % ETEK)	0.5 ± 0.006	0.298 ± 0.003	60 ± 1.9

[a] ORR curves recorded in O_2-saturated 0.1 M $HClO_4$ at 25 °C, sweep rate of 20 mV s^{-1}, and rotation rate of 1600 rpm. Each data point is an average of at least three independent experiments.

The activity of our nanoporous catalysts can be attributed to two characteristics: (1) their residual Ni content and (2) their porous structure/morphology. Pt alloy catalysts, particularly the Ni/Pt alloy, are considerably more active for the ORR than Pt alone; in fact, the $Pt_3Ni(111)$ surface has been found to be the most active surface for the ORR ever discovered with an activity that is 10 times that of Pt(111) and 90 times that of Pt/C catalysts.[14] The improved activity is a consequence of the near surface atomic structure of the Pt alloy; through thermal annealing-induced surface segregation, the alloy surface takes the form of a Pt-skin protecting subsequent atomic layers containing a considerable fraction of Ni or other transition metal. It is this subsurface transition metal that causes a change in the electronic structure of the surface Pt atoms, a down shift in the d-band center, which effectively optimizes the oxygen adsorption strength, ensuring that oxygen binds strong enough to facilitate reduction but also limiting the adsorption of blocking/poisoning hydroxyl species maintaining free and active Pt sites. This effect also has a geometric component where Pt−Pt interatomic spacing can have a dramatic effect on the ORR as seen in the variation in activity with crystallographic orientation where the activity trends with the various low-index facets of Pt_3Ni as (111) > (110) > (100).[14]

Translating this type of surface into a nanoscale fuel cell catalyst context has been achieved to a certain degree through the use of shape-controlled Pt_3Ni alloy nanoparticles. Truncated octahedral Pt_3Ni nanoparticles may be synthesized through careful chemical reduction techniques, allowing control of the proportion of the particular low-index facets where activity was found to increase as the fraction of (111) facets increased.[85,86] Any Ni present on the surface of the alloy particles is quickly removed under potential cycling, creating a Pt-skeleton; however, this skeleton structure may be optimized by varying the initial composition of the alloy nanoparticles where a higher Ni content will result in a thicker shell once the surface is reorganized.[26] Experimental studies on thin films have found that 3 atomic layers of Pt, annealed/smooth skin, over a Ni/Pt alloy yields the highest activity, a trend that has been translated to ∼5 nm Ni/Pt nanoparticles.[7] What is unique about our porous catalyst is that a core−shell, Pt-skeleton structure intrinsically forms during porosity evolution as Pt exposed through Ni dissolution is driven by capillary forces to diffuse along the surface and form Pt-passivated mounds that are eventually undercut, creating interconnected, 3D porosity. Diffusion and aggregation of exposed Pt passivates the surface, protecting the interior of the porous ligaments from the electrolyte and retaining a significant fraction of Ni.[31−33] Residual Ni content in the nanoporous nanoparticles is between 25 and 30 atom %, which is close to the optimal Pt_3Ni composition, and electrochemical hydroxide assays have shown that the surface of the np-NiPt structure is depleted in Ni as dealloying progresses.[33] Taken together, our experimental evidence suggests our nanoporous nanoparticles are composed of a Ni/Pt core-Pt-skeleton shell structure; however, the thickness of the Pt enriched shell along with the degree of atomic surface roughness after potential cycling and electrochemical annealing is as of yet unclear. At the very least, the ORR activity of our core−shell nanoporous nanoparticles agrees well with that for other core−shell nanoparticles of a Pt_3Ni composition[6,21,26,86,87] and are among the highest reported in the literature.

High electrochemical activity in nanoporous electrodes does not necessarily have to be completely attributed to their high surface area to volume ratio; the interconnected, porous geometry can lead to nanoconfinement effects which may result in increased attempt frequencies and improved kinetics. The nanoporous structure is essentially acting as a nanoreactor, increasing the residence time of reactant molecules near the electrode surface by confining them in a 3D porous network where separation between reactive catalyst surfaces is small enough for molecular movement to fall within the Knudsen diffusive regime.[30] Higher residence times result in increased collision frequency, which enhances the probability of a reactant molecule undergoing an electron transfer leading to an enhancement in electrochemical kinetics. This enhancement, however, is limited to reactions occurring in a kinetically or electron transfer-limited regime. In this case, the reaction is slow enough to allow diffusion of reactant molecules from the bulk electrolyte into the depths of the porous network, making the whole of the available nanoporous surface potentially active. For highly reactive molecules such as oxygen, when there is a higher driving force for electron transfer, high overpotential, reactant molecules are not able to penetrate into the pores of the nanoporous electrode and quickly react at the external surface of the electrode. In this diffusion-limited case, the majority of the porous surface is not active and the electrochemically active surface area is essentially equivalent to the geometric surface area of the electrode.[27,30,33] Therefore, this must be taken into account when designing truly effective catalysts that will operate in both the kinetic- and the diffusion-limited regimes. The kinetics of the ORR have been studied as a function of pore depth and roughness factor (real surface area normalized by geometric surface area) in order to determine the proper balance between surface area and reactant diffusion.[27,30,33] For electrodeposited porous Pt films with pore sizes on the order of 10 nm[87] and our own np-NiPt planar electrodes[33] the ORR activity in the mixed kinetic- and diffusion-limited region was found to increase with roughness up to porous depths of approximately 200 nm, above which the activity leveled off. This means that the porous surface beyond a depth of ∼200 nm will be inactive for the ORR and a waste of catalyst mass. This maximum porous depth is well beyond that of our porous particles, and therefore, they should not suffer to a great extent from mass transport losses through the catalyst. The effect of nanoporosity or nanoconfinement on ORR activity can be seen in Figure 11 and Table 4, where we compare nanoporous nanoparticles, 15 nm np-NiPt, to solid particles, 8 nm Ni/Pt, with nearly identical residual Ni compositions, while the ECSA for the solid 8 nm particles is considerably higher than that for the porous nanoparticles. The improvement in activity for the porous particles even with a lower ECSA can be tentatively attributed to the confinement effect within the nanoporous nanoparticles.

4. CONCLUSIONS

In summary, we developed a new type of high surface area, nanoparticulate catalyst composed of nanporous Ni/Pt nanoparticles which are made through dealloying of Ni-rich Ni/Pt alloy nanoparticles. Through manipulation of the nucleation rate during solvothermal synthesis we demonstrated a methodology for obtaining reliable, repeatable control of particle size, allowing us to create Ni-rich alloy particles with diameters greater than 20 nm while maintaining an adequate size distribution. Using this synthesis procedure we were able to experimentally demonstrate the relationship between initial particle size and porosity evolution. We find that porosity evolution requires particle diameters of approximately 15 nm, below which the surface will quickly passivate in Pt during the initial stages of dissolution, preventing penetration of the etch front into the interior of the particle. The high ORR activity for the nanoporous nanoparticles can be attributed to their high surface area to volume ratio, to a core−shell, Pt-skeleton structure with high residual Ni composition, and also to possible nanoconfinement of reactant molecules leading to increased attempt frequencies.

■ AUTHOR INFORMATION

Corresponding Author

E-mail: jonah.erlebacher@jhu.edu

Notes

The authors declare no competing financial interest.

■ ACKNOWLEDGMENTS

We gratefully acknowledge support for this work by the U.S. Department of Energy, Office of Basic Energy Sciences under grant DE-FG02-05ER15727.

REFERENCES

(1) Gasteiger, H.; Kocha, S.; Sompalli, B.; Wagner, F. *Appl. Catal., B* **2005**, *56*, 9−35.

(2) Nocera, D. *ChemSusChem* **2009**, *2*, 387−390.

(3) Gewirth, A.; Thorum, M. *Inorg. Chem.* **2010**, *49*, 3557−3566.

(4) Wagner, F.; Lakshmanan, B.; Mathias, M. *J. Phys. Chem. Lett.* **2010**, *1*, 2204−2219.

(5) Paulus, U.; Schmidt, T.; Gasteiger, H.; Behm, R. *J. Electroanl. Chem.* **2001**, *495*, 134−145.

(6) Stamenkovic, V.; Mun, B.; Arenz, M.; Mayrhofer, K.; Lucas, C.; Wang, G.; Ross, P.; Markovic, N. *Nat. Mater.* **2007**, *6*, 241−247.

(7) Wang, C.; Chi, M.; Li, D.; Strmcnik, D.; van der Vliet, D.; Wang, G.; Komanicky, V.; Chang, K.; Pauliks, A.; Tripkovic, D.; Pearson, J.; More, K.; Markovic, N.; Stamenkovic, V. *J. Am. Chem. Soc.* **2011**, *133*, 14396−14403.

(8) Adzic, R.; Zhang, J.; Sasaki, K.; Vukmirovic, M.; Shao, M.; Wang, J.; Nilekar, A.; Mavrikakis, M.; Valerio, J.; Uribe, F. *Top. Catal.* **2007**, *46*, 249−262.

(9) Sasaki, K.; Kuttiyiel, K.; Su, D.; Adzic, R. *Electrocatalyst* **2011**, *2*, 134−140.

(10) Chen, Y.; Liang, Z.; Yang, F.; Liu, Y.; Chen, S. *J. Phys. Chem. C* **2011**, *115*, 24073−24079.

(11) Strasser, P.; Koh, S.; Anniyev, T.; Greeley, J.; More, K.; Yu, C.; Liu, Z.; Kaya, S.; Nordlund, D.; Ogasawara, H.; Toney, M.; Nilsson, A. *Nat. Chem.* **2010**, *2*, 454−460.

(12) Wang, J.; Inada, H.; Wu, L.; Zhu, Y.; Choi, Y.; Liu, P.; Zhou, W.; Adzic, R. *J. Am. Chem. Soc.* **2009**, *131*, 17298−17302.

(13) Yang, H. *Angew. Chem., Int. Ed.* **2011**, *50*, 2674−2676.

(14) Stamenkovic, V.; Fowler, B.; Mun, B.; Wang, G.; Ross, P.; Lucas, C.; Markovic, N. *Science* **2007**, *315*, 493−497.

(15) Greeley, J.; Stephens, I.; Bondarenko, A.; Johansson, T.; Hansen, H.; Jaramillo, T.; Rossmeisl, J.; Chorkendorff, I.; Norskov, J. *Nat. Chem.* **2009**, *1*, 552−556.

(16) Stamenkovic, V.; Mun, B.; Mayrhofer, K.; Ross, P.; Markovic, N. *J. Am. Chem. Soc.* **2006**, *128*, 8813−8819.

(17) Gong, K.; Chen, W.; Sasaki, K.; Su, D.; Vukmirovic, M.; Zhou, W.; Izzo, E.; Perez-Acosta, C.; Hirunsit, P.; Balbuena, P.; Adzic, R. *J. Electroanal. Chem.* **2010**, *649*, 232−237.

(18) Sasaki, K.; Wang, J.; Naohara, H.; Marinkovic, N.; More, K.; Inada, H.; Adzic, R. *Electrochim. Acta* **2010**, *55*, 2645−2652.

(19) Sasaki, K.; Naohara, H.; Cai, Y.; Choi, Y.; Liu, P.; Vukmirovic, M.; Wang, J.; Adzic, R. *Angew. Chem., Int. Ed.* **2010**, *49*, 8602−8607.

(20) Chen, S.; Sheng, W.; Yabuuchi, N.; Ferreira, P.; Allard, L.; Shao-Horn, Y. *J. Phys. Chem. C* **2009**, *113*, 1109−1125.

(21) Kim, J.; Lee, S.; Carlton, C.; Shao-Horn, Y. *Electrochem. Solid-State Lett.* **2011**, *14*, B110−B113.

(22) Jeon, T.; Yoo, S.; Cho, Y.; Kang, S.; Sung, Y. *Electrochem. Commun.* **2010**, *12*, 1796−1799.

(23) Oezaslan, M.; Hasche, F.; Strasser, P. *J. Electrochem. Soc.* **2012**, *159*, B394−B405.

(24) Hasche, F.; Oezaslan, M.; Strasser, P. *J. Electrochem. Soc.* **2012**, *159*, B25−B34.

(25) Koh, S.; Strasser, P. *J. Am. Chem. Soc.* **2007**, *129*, 12624−12625.

(26) Wang, C.; Chi, M.; Wang, G.; van der Vliet, D.; Li, D.; More, K.; Wang, H.; Schlueter, J.; Markovic, N.; Stamenkovic, V. *Adv. Funct. Mater.* **2011**, *21*, 147−153.

(27) Han, J.; Lee, E.; Park, S.; Chang, R.; Chung, T. *J. Phys. Chem. C* **2010**, *114*, 9546−9553.

(28) Mahmoud, M.; Saira, F.; El-Sayed, M. *Nano Lett.* **2010**, *10*, 3764−3769.

(29) Martinez de la Hoz, J.; Balbuena, P. *J. Phys. Chem. C* **2011**, *115*, 21324−21333.

(30) Bae, J.; Han, J.; Chung, T. *Phys. Chem. Chem. Phys.* **2012**, *14*, 448−463.

(31) Erlebacher, J. *J. Electrochem. Soc.* **2004**, *151*, C614−C626.

(32) Erlebacher, J.; Aziz, M.; Karma, A.; Dimitrov, N.; Sieradzki, K. *Nature* **2001**, *410*, 450−453.

(33) Snyder, J.; Fujita, T.; Chen, M. W.; Erlebacher, J. *Nat. Mater.* **2010**, *9*, 904−907.

(34) Oezaslan, M.; Heggen, M.; Strasser, P. *J. Am. Chem. Soc.* **2012**, *134*, 514−524.

(35) Dubau, L.; Durst, J.; Maillard, F.; Guetaz, L.; Chatenet, M.; Andre, J.; Rossinot, E. *Electrochim. Acta* **2011**, *56*, 10658−10667.

(36) Dutta, I.; Carpenter, M.; Balogh, M.; Ziegelbauer, J.; Moylan, T.; Atwan, M.; Irish, N. *J. Phys. Chem. C* **2010**, *114*, 16309−16320.

(37) Shao, M.; Shoemaker, K.; Peles, A.; Kaneko, K.; Protsailo, L. *J. Am. Chem. Soc.* **2010**, *132*, 9253−9255.

(38) Greeley, J.; Norskov, J. *J. Phys. Chem. C* **2009**, *113*, 4932−4939.

(39) Debe, M.; Steinbach, A.; Vernstrom, B.; Hendricks, S.; Kurkowski, M.; Atanasoski, R.; Kadera, P.; Stevens, D.; Sanderson, R.; Marvel, E.; Dahn, J. *J. Electrochem. Soc.* **2011**, *158*, B910−B918.

(40) van der Vliet, D.; Wang, C.; Debe, M.; Atanasoski, R.; Markovic, N.; Stamenkovic, V. *Electrochim. Acta* **2011**, *56*, 8695−8699.

(41) Wang, D.; Zhao, P.; Li, Y. *Sci. Rep.* **2011**, *1*, 37.

(42) Cai, Y.; Ma, C.; Zhu, Y.; Wang, J.; Adzic, R. *Langmuir* **2011**, *27*, 8540−8547.

(43) Kwon, S.; Hyeon, T. *Small* **2011**, *7*, 2685−2702.

(44) de Mello Donega, C.; Liljeroth, P.; Vanmaekelbergh, D. *Small* **2005**, *1*, 1152−1162.

(45) Wang, D.; Xie, T.; Li, Y. *Nano Res.* **2009**, *2*, 30−46.

(46) Park, J.; Joo, J.; Kwon, S.; Jang, Y.; Hyeon, T. *Angew. Chem., Int. Ed.* **2007**, *46*, 4630−4660.

(47) Tao, A.; Habas, S.; Yang, P. *Small* **2008**, *4*, 310−325.

(48) Wang, D.; Peng, Q.; Li, Y. *Nano Res.* **2010**, *3*, 574−580.

(49) Ren, J.; Tilley, R. *J. Am. Chem. Soc.* **2007**, *129*, 3287−3291.

(50) Wang, C.; Daimon, H.; Lee, Y.; Kim, J.; Sun, S. *J. Am. Chem. Soc.* **2007**, *129*, 6974−6975.

(51) Yin, A.; Min, X.; Zhang, Y.; Yan, C. *J. Am. Chem. Soc.* **2011**, *133*, 3816−3819.

(52) Wu, J.; Gross, A.; Yang, H. *Nano Lett.* **2011**, *11*, 798−802.

(53) Zhang, J.; Fang, J. *J. Am. Chem. Soc.* **2009**, *131*, 18543−18547.

(54) Xia, Y.; Xiong, Y.; Lim, B.; Skrabalak, S. *Angew. Chem., Int. Ed.* **2009**, *48*, 60−103.

(55) Wu, J.; Yang, H. *Nano Res.* **2011**, *4*, 72−82.

(56) Casula, M.; Jun, Y.; Zaziski, D.; Chan, E.; Corrias, A.; Alvisatos, A. P. *J. Am. Chem. Soc.* **2006**, *128*, 1675−1682.

(57) Shevchenko, E.; Talapin, D.; Schnablegger, H.; Kornowski, A.; Festin, O.; Svedlindh, P.; Haase, M.; Weller, H. *J. Am. Chem. Soc.* **2003**, *125*, 9090−9101.

(58) Timonen, J.; Seppala, E.; Ikkala, O.; Ras, R. *Angew. Chem., Int. Ed.* **2011**, *50*, 2080−2084.

(59) Yin, Y.; Alivisatos, A. P. *Nature* **2005**, *437*, 664−670.

(60) Li, Y.; Liu, J. *Chem. Mater.* **2001**, *13*, 1008−1014.

(61) LaMer, V.; Dinegar, R. *J. Am. Chem. Soc.* **1950**, *72*, 4847−4854.

(62) Watzky, M.; Finke, R. *J. Am. Chem. Soc.* **1997**, *119*, 10382−10400.

(63) Finney, E.; Finke, R. *J. Colloid Interface Sci.* **2008**, *317*, 351−374.

(64) Lee, S.; Cho, S.; Cheon, J. *Adv. Mater.* **2003**, *15*, 441−444.

(65) Zhang, H.; Li, W.; Jin, M.; Zeng, J.; Yu, T.; Yang, D.; Xia, Y. *Nano Lett.* **2011**, *11*, 898−903.

(66) Sau, T.; Rogach, A. *Adv. Mater.* **2010**, *222*, 1781−1804.

(67) Gong, S.; Lu, J.; Yan, H. *J. Electroanal. Chem.* **1997**, *436*, 291−293.

(68) Garsany, Y.; Baturina, O.; Swider-Lyons, K.; Kocha, S. *Anal. Chem.* **2010**, *82*, 6321−6328.

(69) Garsany, Y.; Singer, I.; Swider-Lyons, K. *J. Electroanal. Chem.* **2011**, *662*, 396−406.

(70) van der Vliet, D.; Strmcnik, D.; Wang, C.; Stamenkovic, V.; Markovic, N.; Koper, M. *J. Electroanal. Chem.* **2010**, *647*, 29−34.

(71) Shevchenko, E.; Talapin, D.; Rogach, A.; Kornowski, A.; Haase, M.; Weller, H. *J. Am. Chem. Soc.* **2002**, *124*, 11480−11485.

(72) Ahrenstorf, K.; Albrecht, O.; Heller, H.; Kornowski, A.; Gorlitz, D.; Weller, H. *Small* **2007**, *3*, 271−274.

(73) Cuya Huaman, J.; Fukao, S.; Shinoda, K.; Jeyadevan, B. *CrystEngComm* **2011**, *13*, 3364−3368.

(74) Wang, D.; Li, Y. *J. Am. Chem. Soc.* **2010**, *132*, 6280−6281.

(75) Wang, D.; Li, Y. *Inorg. Chem.* **2011**, *50*, 5196−5202.

(76) Cheon, J.; Kang, N.; Lee, S.; Lee, J.; Yoon, J.; Oh, S. *J. Am. Chem. Soc.* **2004**, *126*, 1950−1951.

(77) Wang, C.; Daimon, H.; Onodera, T.; Koda, T.; Sun, S. *Angew. Chem., Int. Ed.* **2008**, *47*, 3588−3591.

(78) Wang, C.; van der Vliet, D.; Chang, K.; You, H.; Strmcnik, D.; Schlueter, J.; Markovic, N.; Stamenkovic, V. *J. Phys. Chem. C* **2009**, *113*, 19365−19368.

(79) Wang, C.; Wang, G.; van der Vliet, D.; Chang, K.; Markovic, N.; Stamenkovic, V. *Phys. Chem. Chem. Phys.* **2010**, *12*, 6933−6939.

(80) Tang, L.; Li, X.; Cammarata, R.; Friesen, C.; Sieradzki, K. *J. Am. Chem. Soc.* **2010**, *132*, 11722−11726.

(81) Tang, L.; Han, B.; Persson, K.; Friesen, C.; He, T.; Sieradzki, K.; Ceder, G. *J. Am. Chem. Soc.* **2010**, *132*, 596−600.

(82) McCue, I.; Snyder, J.; Li, X.; Chen, Q.; Sieradzki, K.; Erlebacher, J. *Phys. Rev. Lett.*, in press.

(83) Wang, C.; Chi, M.; Li, D.; van der Vliet, D.; Wang, G.; Lin, Q.; Mitchell, J.; More, K.; Markovic, N.; Stamenkovic, V. *ACS Catal.* **2011**, *1*, 1355−1359.

(84) Fuel Cell Technologies Program, *Mulit-Year Research, Development and Demonstration Plan*, http://www1.eere.energy.gov/hydrogenandfuelcells/mypp/pdfs/fuel_cells.pdf.

(85) Zhang, J.; Yang, H.; Fang, J.; Zou, S. *Nano Lett.* **2010**, *10*, 638−644.

(86) Wu, J.; Zhang, J.; Peng, Z.; Yang, S.; Wagner, F.; Yang, H. *J. Am. Chem. Soc.* **2010**, *132*, 4984−4985.

(87) Park, S.; Song, Y.; Han, J.; Boo, H.; Chung, T. *Electrochim. Acta* **2010**, *55*, 2029−2035.